SAND2000-0439J

Solute transport in variable aperture fractures: An investigation of the relative importance of Taylor dispersion and macrodispersion

Russell L. Detwiler[1], Harihar Rajaram[1], Robert J. Glass[2]
[1] Department of Civil, Environmental, and Architectural Engineering, University of Colorado, Boulder, Colorado 80309-0428. e-mail: detwiler@thaneer.colorado.edu, hari@thaneer.colorado.edu.
[2] Flow Visualization and Processes Laboratory, Sandia National Laboratories, Albuquerque, New Mexico 87123-1345. e-mail: rjglass@sandia.gov.

Abstract

Dispersion of solutes in a variable aperture fracture results from a combination of molecular diffusion and velocity variations in both the plane of the fracture (macrodispersion) and across the fracture aperture (Taylor dispersion). We use a combination of physical experiments and computational simulations to test a theoretical model in which the effective longitudinal dispersion coefficient, D_L, is expressed as a sum of the contributions of these three dispersive mechanisms. The combined influence of Taylor dispersion and macrodispersion results in a nonlinear dependence of D_L on the Peclet number (Pe=V<b>/Dm, where V is the mean solute velocity, <b> is the mean aperture and D_m is the molecular diffusion coefficient). Three distinct dispersion regimes become evident: for small Pe (Pe<<1), molecular diffusion dominates resulting in $D_L \propto Pe^0$; for intermediate Pe, macrodispersion dominates ($D_L \propto Pe$); and for large Pe, Taylor dispersion dominates ($D_L \propto Pe^2$). The Pe-range corresponding to these different regimes is controlled by the statistics of the aperture field. In particular, the upper limit of Pe corresponding to the macrodispersion regime increases as the macrodispersivity increases. Physical experiments in an analog, rough-walled fracture, confirm the nonlinear Pe-dependence of D_L predicted by the theoretical model. However, the theoretical model underestimates the magnitude of D_L. Computational simulations, using a particle tracking algorithm that incorporates all three dispersive mechanisms, agree very closely with the theoretical model predictions. The close agreement between the theoretical model and computational simulations is largely because, in both cases, the Reynolds equation describes the flow field in the fracture. The discrepancy between theoretical model predictions and D_L estimated from the physical experiments appears to be largely due to deviations from the local cubic law assumed by the Reynolds equation.

DISCLAIMER

DISCLAIMER

Portions of this document may be illegible in electronic image products. Images are produced from the best available original document.

1. Introduction

Solute transport in a rough-walled fracture is controlled by diffusive and advective processes. The Peclet number, $Pe = Vb/D_m$, where V is the mean solute velocity, b is a characteristic length scale (e.g., fracture aperture), and D_m is the molecular diffusion coefficient, defines the relative importance of each transport process. Molecular diffusion dominates for $Pe<<1$. Within the advection-dominated regime (larger Pe values), two different mechanisms lead to dispersion due to variable velocity within the rough walled geometry: Taylor dispersion and macrodispersion. Taylor dispersion results from mixing induced by velocity variations across the fracture aperture. Macrodispersion is caused by velocity variations in the plane of the fracture that result from aperture variability. Because of their different origins, Taylor dispersion and macrodispersion exhibit different fundamental dependence on Pe, with Taylor dispersion proportional to Pe^2 and macrodispersion proportional to Pe.

Computational simulations of transport in fractures have incorporated the influence of either Taylor dispersion [i.e., parallel plate fractures, e.g., Hull et al., 1987; Ippolito et al., 1994] or macrodispersion [i.e. constant velocity across the fracture aperture, e.g., Moreno et al., 1988; Thompson, 1991; Thompson and Brown, 1991], but not both. Recent experimental evidence [Ippolito et al., 1994] and scaling analyses [Roux et al., 1998] suggest that dispersion in variable-aperture fractures can be described as a sum of molecular diffusion, Taylor dispersion, and macrodispersion. Roux et al. [1998] also presented scaling arguments suggesting that the Pe-range within which each dispersion process dominates, is controlled by the mean, variance, and correlation scale of the aperture field.

To date, there are no experimental or computational studies that fully delineate the various regimes of solute dispersion in variable aperture fractures. Ippolito et al. [1994] experimentally demonstrated the influence of two distinct dispersion regimes (i.e., Taylor dispersion and macrodispersion). However, they did not quantify the statistics of the aperture field in their experimental fracture, making it difficult to generalize their results. Keller et al. [1995] and Keller et al. [1999] measured the longitudinal dispersion coefficient, D_L, over a range of Pe in two different natural fractures in granite. They compared these results to D_L predicted using stochastic theory and the measured statistics of their aperture fields. However, large-scale aperture variability (clearly evident in images of the aperture fields in both of their fractures) likely dominated the dispersion process, partially invalidating comparisons of experimental results to stochastic theory. Dronfield and Silliman [1993] demonstrated a nonlinear relationship between D_L and Pe ($D_L \propto Pe^{-1.4}$), based on transport experiments in a sand-roughened analog fracture. This result suggests that their experiments (run over a narrow range of Pe) were in the transition zone between Taylor dispersion and macrodispersion.

In this paper, we use a combination of physical experiments and computational simulations to explore the Pe-ranges of the different dispersion regimes, as controlled by the mean, variance, and correlation scale of the aperture field. We also present a theoretical expression for D_L that combines Taylor dispersion and macrodispersion. Our experiments use a light transmission technique that yields high resolution, accurate measurements of both aperture fields and solute concentration fields in transparent analog fractures. This approach offers the advantages that the aperture field is measured at the time of the experiment and dispersion of a dye pulse within the fracture is followed directly, avoiding assumptions about mixing in the inflow and outflow manifolds that are required when estimating D_L from breakthrough curves measured at the outflow. Our computational model tracks particles through a variable aperture fracture. The velocity field within the fracture is

specified using a parabolic velocity profile across the aperture, where the local, aperture-averaged velocity is obtained from a numerical solution of the Reynolds equation. In addition to advection within this three-dimensional velocity field, particles undergo three-dimensional molecular diffusion. Thus, the mechanisms that cause both Taylor dispersion and macrodispersion are incorporated into the model.

We first performed experiments in a Hele-Shaw cell (flat, parallel-plate fracture) and used the results to verify our computational model in the absence of aperture variation and to measure D_m for our solute. We then experimentally investigated the range of Pe where the transition between macrodispersion and Taylor dispersion occurs in a rough-walled fracture. To transcend experimental limitations and explore Taylor dispersion and macrodispersion regimes over a wide range of Pe for aperture fields with different statistics, we designed a sequence of computational simulations. First we compared our modeling approach to the experiments to evaluate model error and then simulated a much wider Pe-range within a synthetic aperture field with similar statistics to our experimental fracture. Finally, we simulated transport through two additional synthetic aperture fields to consider the influence of aperture variance and correlation length on the Pe range over which the different dispersion mechanisms dominate.

Our simulations support the Roux et al. [1998] scaling estimates of the Pe range corresponding to the relative dominance of Taylor dispersion and macrodispersion. The theoretical expression for D_L, which is a sum of the macrodispersion coefficient [Gelhar, 1987, 1993] and Taylor dispersion coefficient, and shares the fundamental assumptions of the Reynolds equation, agrees closely with our computational results. However, for our rough-walled experimental fracture, theoretical estimates of D_L are significantly less than the experimentally measured values (e.g., by 51% at Pe = 300). We believe that this discrepancy between experiment and theory is primarily due to the inability of the Reynolds equation, upon which the stochastic theory is based, to fully describe the velocity field within a rough-walled fracture [e.g., Yeo et al., 1998; Nicholl et al., 1999]

2. Theoretical description of dispersion in variable aperture fractures

In a parallel-plate fracture, the primary mechanism causing dispersion is the well-known phenomenon of Taylor dispersion [Taylor, 1953; Aris, 1956]. The Taylor dispersion coefficient for a parallel-plate fracture is [e.g., Fischer et al., 1979]:

$$D_{L,Taylor} = \frac{V^2 b^2}{210\, D_m} \qquad (1a)$$

where V is the average velocity in the fracture, b is the fracture aperture, and D_m is the molecular diffusion coefficient.

For transport in a variable-aperture fracture, Gelhar [1987, 1993] developed a stochastic analysis of flow and solute transport. Gelhar's analysis assumes that the logarithm of the aperture (β=ln b) is a statistically stationary, gaussian, random field, and that the flow within a variable-aperture can be described by the Reynolds equation. The Reynolds equation is based on the assumptions that aperture variations are relatively smooth and the velocity profile across the aperture is parabolic, corresponding to local, plane Poisseuille flow [e.g., Zimmerman and Bodvarsson, 1996]. The stochastic analysis of flow reveals that the effective hydraulic aperture is equal to the geometric mean aperture. The stochastic transport analysis neglects the influence of local dispersion and results in the following expression for the macrodispersion coefficient:

$$D_{L,macro} = \sigma_\beta^2 \lambda [3 + I(\sigma_\beta{}^2)/\sigma_\beta{}^2] V = \sigma_\beta^2 \lambda B V \qquad (2a)$$

In (2a), σ^2_β and λ are the variance and integral scale of β, respectively,

$$B = 3 + I(\sigma_\beta{}^2)/\sigma_\beta{}^2 \qquad (3)$$

and

$$I(\sigma_\beta{}^2) = \frac{1}{\pi}\int_0^\infty [\exp(R_{\beta\beta}(u)) - 1]\, du \qquad (4)$$

where $R_{\beta\beta}(u)$ is the covariance function of β, u is the nondimensional spatial separation variable, which equals the spatial separation divided by λ. Note that for an exponential covariance, λ is equivalent to the correlation length, or the length-scale over which correlation in β persists. Also note that V in (2a) is the mean solute velocity, equal to the mean flux through the fracture divided by the mean aperture (<b>) [Gelhar, 1993]. The expression (2a) incorporates the influence of variations in the mean flow velocity within the fracture plane, but not the influence of Taylor dispersion. Equations (1a) and (2a) demonstrate that $D_{L,macro}$ is proportional to V and $D_{L,Taylor}$ is proportional to V^2, which suggests that at high flow rates, Taylor dispersion may dominate over macrodispersion, even in a variable aperture fracture.

The expressions (1a) and (2a) may be rewritten in a nondimensional form, in terms of Pe = V<b>/D_m, where <b> is the mean aperture and V is the mean solute velocity:

$$\frac{D_{L,Taylor}}{D_m} = \frac{Pe^2}{210} = \alpha_{Taylor} Pe^2 \qquad (1b)$$

$$\frac{D_{L,macro}}{D_m} = \frac{\sigma_\beta^2 \lambda B}{\langle b \rangle} Pe = \alpha_{macro}\, Pe \qquad (2b)$$

In (1b) and (2b), α_{Taylor} and α_{macro} are nondimensional coefficients for the contributions of Taylor dispersion and macrodispersion, respectively. Note that (1b) represents an "effective" Taylor dispersion coefficient in a rough-walled fracture based on the mean aperture and mean solute velocity. A stochastic analysis of Taylor dispersion in a variable aperture fracture is required to establish the validity of such a representation of the effective Taylor dispersion coefficient.

Roux et al. [1998] used scaling arguments to suggest three primary dispersion regimes in variable-aperture fractures: molecular diffusion, "geometric" dispersion and Taylor dispersion. The "geometric" dispersion regime corresponds to the range of Pe where velocity variations in the plane of the fracture dominate the mixing process and $D_L \propto Pe$. We note that this is equivalent to macrodispersion as described by (2a,b) and we use the latter term to refer to this regime in the remainder of the paper. Roux et al. [1998] used scaling relationships for D_L in the Taylor dispersion and macrodispersion regimes to define the approximate Pe range within which macrodispersion is the dominant dispersion mechanism. However, they did not use the precise relationships (1b) and (2b) to quantify the macrodispersion and Taylor dispersion coefficients. Roux et al. [1998] also suggested that D_L can be expressed as a sum of the three different components. This results in a first order approximation of the total nondimensional longitudinal dispersion coefficient of the form:

$$\frac{D_L}{D_m} = \tau + \alpha_{macro} Pe + \alpha_{Taylor} Pe^2 \qquad (5)$$

where τ is the tortuosity for diffusion within the fracture, typically <1.0, reflecting the reduced rate of molecular diffusion in a geometrically complex void space. For typical Pe ranges, τ is an insignificant contribution to D_L/D_m and may be dropped from (5). Equation (5) suggests that α_{macro} will be influenced by the statistics of the aperture field and will increase with σ_β^2 and $\lambda/\langle b \rangle$. Additionally, the Pe-range over which macrodispersion can be expected to dominate is:

$$1/\alpha_{macro} < Pe < \alpha_{macro}/\alpha_{Taylor} \qquad (6)$$

where τ is assumed to be approximately 1.

Figure 1 shows D_L/D_m, from (5), plotted against Pe for two hypothetical values of α_{macro} (0.2 and 20) with τ and α_{Taylor} equal to 1 and 1/210, respectively. The curve for α_{macro} = 0.2 transitions directly from a molecular diffusion regime (slope = 0) to the Taylor

dispersion regime (slope = 2) whereas the curve for $\alpha_{macro} = 20$ exhibits a large region, $O(10^{-1})<Pe<O(10^{4})$, where macrodispersion dominates (slope = 1). To highlight these different dispersion regimes, it is useful to plot D_L in the nondimensional form $D_L/(V<b>)$ against Pe (**Figure 2**). **Figures 1** and **2** demonstrate the importance of quantifying α_{macro} to determine the Pe-range associated with the different dispersion regimes in a given fracture.

To fully study the Pe-range corresponding to different dispersion regimes, requires a fracture that is long compared to λ. Theoretical results for a two-dimensional, isotropic, random field with exponential covariance suggest that D_L should reach 99% of its asymptotic value after the solute has traveled a distance of ~20λ [e.g., Dagan, 1984]. Similarly, for transport between parallel plates, Taylor dispersion should become fully developed at a distance of ~$0.4<b>Pe$ [e.g., Fischer et al., 1979]. Thus to make a meaningful comparison of physical and computational experiments to theory, we require a stationary field with small λ compared to the dimensions of the field. This ensures that D_L will become relatively constant within the scale of the experiment. We also require a source whose transverse dimensions extend over ~20λ to eliminate non-ergodic effects. However, to avoid an increase in Taylor dispersion due to the velocity variations at the lateral boundaries of the fracture [e.g. Doshi et al., 1977], the source should also be narrow compared to the width of the fracture. These issues were considered in the design of our experimental fracture, discussed in detail in Section 3.

In the remainder of the paper, we use experimental and computational results to measure values of α_{Taylor} and α_{macro} as given by (1b) and (2b) and to investigate the corresponding transitions between the different dispersion regimes: Section 3 discusses experimental results over the full Pe-range obtainable with our experimental system; Section 4 describes our computational experiments both in the experimentally measured field and in synthetic fields generated with different σ_β^2 and λ; and Section 5 compares estimates of D_L obtained from physical and computational experiments to theoretical estimates based on (5).

3. Experimental investigations

We carried out experiments in two analog fractures: a Hele-Shaw cell fabricated from two pieces of flat glass and a rough-walled fracture fabricated by mating two pieces of textured glass (fabrication details for both fractures are described by Nicholl et al. [1999]). **Table 1** presents the dimensions of each of the fractures. Experiments in the Hele-Shaw cell provided a test for our computational model as well as a measurement of D_m. The rough-walled fracture was designed to have a stationary, isotropic aperture field with a correlation scale much smaller than the dimensions of the fracture and values of σ_β^2 and <b> in the range of values reported for natural fractures. These transparent analog fractures offered the additional advantage of allowing direct, full-field aperture and solute concentration measurements, with no disturbance of the fracture between the aperture measurements and transport experiments. Thus our experiments can be directly compared to computational simulations and theoretical results.

A test cell frame supported the fractures and allowed light from a feedback controlled source to be transmitted through the entire fracture (**Figure 3a**). An electronically cooled, 12-bit, shuttered, charge-coupled-device (CCD) camera (2045 x 2033 pixels, 4096 gray levels) supported above the test cell measured the intensities of transmitted light. We measured aperture fields and solute concentration fields using a light transmission technique first proposed by Glass et al. [1991]. The details of the experimental system, the aperture measurement technique, and a method for quantifying aperture errors are presented by Detwiler et al. [1999].

3.1. Measurement techniques

A light absorbing dye (Warner Jenkins FD&C Blue #1 dye) was used both as a tracer during transport experiments and as a light absorbing solute for aperture measurement. The Beer-Lambert law describes the absorbance of monochromatic light by a dyed solution as a function of the distance through the solution (b) and the dye concentration (C). According to the Beer-Lambert law, the absorbance at each pixel (identified using a double subscript 'ij', where i and j refer to the row and column index of the pixel) within a two-dimensional field is given by:

$$A_{ij} = \ln\left(I_{cl_{ij}} / I_{dye_{ij}}\right) = \mu C_{ij} b_{ij} \qquad (7)$$

where A_{ij} is the absorbance, $I_{cl_{ij}}$ and $I_{dye_{ij}}$ are the intensities transmitted through a clear and a dyed solution, respectively, μ is the absorptivity of the solute, C_{ij} is the dye concentration, and b_{ij} is the thickness of the absorbing layer or the local aperture. Images of a fracture filled entirely with clear and dyed solutions yield arrays of intensity measurements, $I_{cl_{ij}}$ and $I_{dye_{ij}}$ for use in (7). Normalizing (7) by its mean then gives an expression for the aperture:

$$b_{ij} = A_{ij}\langle b\rangle / \langle A\rangle \qquad (8)$$

where <b> is the independently measured mean aperture and <A> is the mean (over all ij) of A_{ij}. We determined <b> by injecting a known volume of fluid into the fracture and measuring the area occupied by the fluid. Once b_{ij} is calculated for the entire fracture, we

can measure concentrations (C_{ij}) using images taken during transport experiments by directly applying (7).

If the light source is polychromatic, as is the case with our measurement system, the linear relationship between absorbance and concentration (7) is only approximate. Despite efforts to remove the influence of nonlinear absorbance on our measurements by reducing the measured wavelengths with a band pass filter (Andover Corporation, 630 nm ± 5 nm) on the camera lens, some nonlinearity remained. Slight nonlinearity in dye absorbance results in aperture measurement errors that increase with dye concentration, but reducing dye concentration results in an increase in random errors due to signal noise caused by the smaller signal range (i.e. difference between $I_{cl_{ij}}$ and $I_{dye_{ij}}$). We reduced the influence of random errors by averaging 80 images of each field and used the procedure described by Detwiler et al. [1999] to determine the dye concentration for measuring $I_{dye_{ij}}$ (0.05 g/l) that resulted in the minimum total error. We estimated root-mean-square (RMS) aperture measurement errors of 0.8 and 1.2 percent of the mean aperture for the Hele-Shaw cell and the rough-walled fracture, respectively.

For transport experiments, we could not average multiple images, so we used a higher dye concentration that utilized the full dynamic range of the CCD camera. The use of a higher dye concentration reduces the influence of noise on measurements of C_{ij}, thus increasing the sensitivity of our measurements, especially in regions of low concentration (i.e., solute plume tails). However, a higher dye concentration also results in nonlinear absorbance in regions of high concentration. We accounted for the influence of nonlinear absorbance on concentration measurements by fitting the following function to a series of measurements made at different dye concentrations (0.025, 0.05, 0.10, 0.15, 0.20, and 0.25 g/l):

$$A_{ij} = e_{ij} C_{ij} / \left(f_{ij} + C_{ij} \right) \qquad (9)$$

In (9), e_{ij} and f_{ij} are fitting parameters determined at each pixel in the array. Note that for low concentrations (i.e. $C_{ij} << f_{ij}$), (9) reduces to a linear relationship similar to (7). To obtain the concentration at each location, we use the fitted parameters e_{ij} and f_{ij} and solve (9) for C_{ij}:

$$C_{ij} = \left(f_{ij} / e_{ij} \right) / \left(1/A_{ij} - 1/e_{ij} \right) \qquad (10)$$

The maximum RMS concentration error at any location is ~$0.023C_o$ (C_o = 0.25 g/l), based on an analysis discussed in detail in the Appendix.

3.2 Measured aperture fields

Table 1 provides a summary of the dimensions and statistics of the two aperture fields. The aperture field for the Hele-Shaw cell exhibits a narrow distribution (variance, $\sigma_b^2 = 2.78 \times 10^{-7}$ cm^2) about its mean (<b>=0.0193 cm). The i and j-semivariograms (long and short principal axes) for the Hele-Shaw cell (**Figure 4**) show a relatively strong trend along the short axis and a milder trend along the long axis. Although the glass plates were flat, clamping pressure resulted in smaller apertures along the edges of the cell (~0.018 cm), larger apertures along the centerline of the cell (0.020 cm), and uneven compression

of the plastic shims along the length of the fracture (**Figure 3b**). These features led to apparent large-scale trends in the aperture field as evident in the variograms shown in **Figure 4**.

The aperture field of the rough-walled fracture has a wider, negatively skewed distribution (see **Figure 8**) with $\sigma_b^2 = 3.62 \times 10^{-5}$ cm^2 and $\langle b \rangle = 0.0221$ cm. Nicholl et al. [1999] present an image of a portion of the rough-walled aperture field. The semivariograms for the rough-walled fracture (**Figure 4**) indicate that the field is isotropic and reaches the level of the sill at a separation of ~0.08 cm. The semivariograms also indicate a slight negative correlation at separations between ~0.08 cm and ~0.18 cm caused by the repetitive nature of the individual fracture surfaces. Numerically integrating the correlation functions of β_{ij} yields estimates of λ of ~0.044 cm along both the long and short axes.

3.3. Transport Experiments

We conducted a series of transport experiments in each fracture, over a range of flow rates. To facilitate reproducibility, a computer controlled flow through the fracture by activating/deactivating solenoid valves, measured flow rates by recording outflow mass at equal intervals, and triggered the CCD camera to acquire images at specified times. Inflow and outflow manifolds provided uniform pressure across the width of the two ends of each fracture and no flow boundaries were applied to the sides of each fracture (**Figure 3**). A constant head reservoir at the inflow and a stabilized drip point at the outflow created steady, reproducible flow rates through the fracture. **Table 2** summarizes the flow rates for each experiment. The CCD camera required ~11 seconds to write each image to disk, so we chose the maximum flow rate for each fracture so that we could acquire at least 10 images (i.e., concentration fields) during an individual transport experiment. The minimum flow rate represents the reproducible limit achievable using the constant head reservoirs of our system.

The initial condition for each experiment is shown in the first frame of **Figures 5a and 5b**. This initial condition provides two advantages: a known initial concentration distribution and negligible edge effects caused by the no flow boundaries of the fracture. We pumped a 0.375 g/l slug of solute through the injection port in the center of the inflow manifold (**Figure 3a**) into the center of the inflow end of the fracture. We then flushed the inflow manifold by pumping clear water into the two ends (i.e., inflow and waste line in **Figure 3a**) and out through the injection port. After flushing the inflow manifold with clear water, we stopped the pump, closed the valve at the waste side of the inflow manifold and opened the outflow manifold, initiating flow through the fracture under constant gradient. In designing the transport experiments we considered the possible influence of gravitational effects on dispersion in the fractures. Relatively small density gradients can lead to enhanced dispersion at early times (i.e. before density gradients are reduced by dispersion) [e.g., Reejhsinghani et al., 1966]. Our results (discussed in Section 3.5) comfirm that density effects were negligible.

Figures 5a and **5b** show sequences of three solute concentration fields from experiments in the Hele-Shaw cell and the rough-walled fracture. The concentration fields demonstrate the initial condition in the first frame and the effect of dispersion on the plumes in the two successive frames. The role of aperture variability in enhancing dispersion is clearly evident in **Figure 5b**. The progressive reduction in the peak concentration is also evident in **Figures 5a and 5b**.

3.4. Analysis of Concentration Fields

The product of a measured solute concentration field and the measured aperture field yields the solute mass at each pixel in the field, and summation over the entire field yields the total mass within the system. The total mass measured in each of the fields obtained during any of the experiments varied by no more than ±3% from the total mass averaged over all fields from a single experiment. Good mass conservation further confirms the accuracy of our measurement techniques. The rates of change of the first and second spatial moments (M_{1x} and M_{2x}, respectively) of solute mass in the flow direction with time are equivalent to the mean solute velocity (V) and twice the longitudinal dispersion coefficient ($2D_L$), respectively [e.g., Aris, 1956]. We calculated M_{1x} for each solute mass field using:

$$M_{1x} = \sum_{i=1}^{nx}\sum_{j=1}^{ny} C_{ij} b_{ij} x_{ij} \Big/ \sum_{i=1}^{nx}\sum_{j=1}^{ny} C_{ij} b_{ij} \qquad (11)$$

where C_{ij}, b_{ij}, and x_{ij} are the concentration, aperture, and x-coordinate at pixel ij and nx and ny are the number of measurements in the x and y-directions. We then calculated M_{2x} for each field using:

$$M_{2x} = \sum_{i=1}^{nx}\sum_{j=1}^{ny} C_{ij} b_{ij} \left(x_{ij} - M_{1x}\right)^2 \Big/ \sum_{i=1}^{nx}\sum_{j=1}^{ny} C_{ij} b_{ij} \qquad (12)$$

We then estimated D_L and V by plotting M_{1x} and M_{2x} against time. Note that this method of measuring D_L requires no assumptions about the initial condition for the experiment. The initial concentration distribution is directly measured. This approach overcomes the difficulties involved in using breakthrough curves and an analytical solution to the one-dimensional advection-diffusion equation for estimating transport parameters. The latter approach assumes initial conditions that are typically difficult to verify and mixing in the inflow and outflow systems leads to inaccuracies in estimates of transport parameters.

3.5. Experimental Results

Experiments in both the Hele-Shaw cell and the rough-walled fracture resulted in linear plots of M_{2x} versus time from the initial concentration field until solute began to exit the fracture. This indicates that the conditions for full development of both macrodispersion and Taylor dispersion described in Section 2 were met at very early times in our experiments. Based on the theory presented in Section 2, the distances required for development of Taylor dispersion (~0.4<b>Pe) and macrodispersion (20λ) are ~0.9 cm and ~0.9 - 7.0 cm, respectively. Linear plots of M_{2x} versus time over the full range of experimental flow rates also confirms that the influence of natural convection due to density gradients was negligible, i.e., no enhanced dispersion was observed at early time (i.e., faster M_{2x} growth), as would be expected with significant natural convection [e.g. Stockman, 1997].

We used the procedures described in Section 3.4 to calculate the mean solute velocity and dispersion coefficient for each experiment (**Table 2**) (the Appendix provides a detailed discussion of errors in our estimates of D_L). For both fractures we demonstrated the reproducibility of our experiments by repeating a number of experiments at one flow

rate (see experiments 5a, b, and c in **Figure 6 and Table 2**). **Figure 6** is a plot of D_L/D_m versus Pe for each set of experiments. The range of Pe values covered by our experiments extends from ~100-800. We determined D_m to be 5.67 x 10^{-6} cm^2/s by fitting (1a), the theoretical expression for Taylor dispersion between parallel plates, to the experimental results from the Hele-Shaw cell. Although, as discussed in Section 3.3, the aperture field in the Hele-Shaw cell is not perfectly uniform (due to bowing of the glass plates), the plates are essentially parallel along the central portion of the cell traversed by the solute plume. Note that this method is analogous to an accepted method for measuring D_m that involves measuring the dispersion of a solute in laminar flow through a tube and using the theoretical expression for Taylor dispersion in a tube to calculate D_m [e.g., Cussler, 1984].

In the rough-walled fracture, the relationship between D_L/D_m and Pe is also non-linear (**Figure 6**), indicating that Taylor dispersion contributes to dispersion over the Pe-range of our experiments. Dropping τ and fitting (5) to our experimental data results in estimates of α_{macro} = 1.87±0.15 and α_{Taylor} = (5.22±0.26) x 10^{-3}. These results, with (6), allow us to estimate the range over which macrodispersion will be the dominant dispersion mechanism as $0.5 \lesssim Pe \lesssim 350$. Because the range over which we can perform experiments in our current system is limited ($100 \lesssim Pe \lesssim 800$), we cannot investigate the full range of Pe-dependence. Additionally we are limited to a single σ_β^2, λ, and <b>, unless we design and fabricate additional aperture fields for experimental investigation.

4. Computational investigations

The theory presented in Section 2 suggests that the nature of the Pe-dependence of D_L will depend on aperture statistics (<b>, σ_β^2, and λ). To investigate the influence of Pe and aperture variability on D_L over a wider range of parameters (Pe, <b>, σ_β^2, and λ) than is possible in a single experimental fracture, we simulate flow and transport through computer-generated aperture fields. Measured aperture and concentration fields from our physical transport experiments allow us to first test the computational model through direct comparison before proceeding to additional computational studies.

4.1. Flow and transport solvers

To simulate the velocity field within the fracture, we used the flow solver developed by Nicholl et al. [1999], which uses a finite difference discretization of the Reynolds equation. We used the harmonic average (found by Nicholl et al. [1999] to agree more closely with experimental results than several other variations) to define the transmissivities between adjacent grid blocks. For comparison to our experimental results, we used a grid that corresponded to the measured aperture field (e.g., 958 x 1958 with dimensions of each grid block equal to 0.0154 x 0.0154 cm); this is approximately the same discretization used by Nicholl et al. [1999] for this fracture.

Nicholl et al. [1999] compared flow computations made with this flow solver to saturated flow experiments in the two fractures used in this study, as well as a third fracture fabricated by mating a single piece of rough glass with a single piece of smooth glass. Their comparison indicated that the Reynolds equation (and other two-dimensional variants that account for convergence/divergence of flow and tortuosity of the centerline) overestimates flow through the rough-walled fracture used in the current study by ~26%. High-resolution simulations on a subset of the entire field indicated that increasing the resolution of aperture measurements, and subsequently the finite difference grid, had a negligible influence (~2%) on the results. Thus, they concluded that it may be necessary to solve the three-dimensional Stokes equations in situations where improved accuracy is required. Because the Reynolds equation overestimates flow under a specified gradient in rough-walled fractures, we specified the mean flux to generate the flow fields for transport simulations resulting in simulated mean solute velocities that closely matched our experimentally measured means.

We simulated solute transport using a three-dimensional random-walk particle tracking algorithm. We used the same discretization of the domain used for solving the Reynolds equation and assumed that the aperture within each grid block was constant. This is consistent with experimental aperture measurements that represent an average of the aperture within each pixel. In addition, our measurement system only provides measurements of the local aperture, and not deviations of the local aperture midpoint from the center-plane of the fracture. For the transport simulations, we assume that the fracture is symmetric about the center-plane to approximate the actual fracture geometry. However, it should be noted that when the assumptions underlying the Reynolds equation are satisfied, the flow field depends only on the aperture field and not explicitly on the geometry of the fracture surfaces. Particle displacements in each time step consisted of a two-dimensional advective displacement (in the x,y plane) and a three-dimensional random diffusive displacement (x,y,z, where z is across the aperture) reflecting the role of molecular diffusion. We calculated the advective displacements using the local gradients specified by the solution to the Reynolds equation and imposing a parabolic velocity profile across the

local aperture. In the absence of diffusion, particles maintained their relative z-position, creating a pseudo-advection in the z-direction when a particle moved between adjacent grid blocks with different apertures. Particles colliding with the fracture wall due to diffusion across the aperture were reflected back into the fracture. Adaptive time stepping ensured that the three-dimensional velocity field was well sampled by each particle. The minimum of the following three criteria defined the length of each time step: the time required for a mean diffusive displacement of 5% of the local aperture and the times required for a particle traveling at the maximum local velocity (i.e. along the aperture centerline) to traverse 50% of the local grid block in both the x and y-directions.

4.2 Comparison of results from physical experiments and computational simulations

Accurate, full-field measurements of both aperture and concentration allow us to directly compare the results of the computational simulations to the experimental data. We specified initial particle locations based on the initial conditions in our experiments. The initial conditions were generated by taking the initial solute mass field from an experiment and assigning a specific mass to each particle (5.0×10^{-10} gm for the Hele-Shaw cell and 2.5×10^{-10} gm for the rough-walled fracture) resulting in a total of $\sim 3.0 \times 10^4$ particles for the Hele-Shaw cell and $\sim 3.5 \times 10^4$ particles for the rough-walled fracture. The particles were then randomly distributed within the grid block specified by their initial location. **Figure 5c** shows images of simulated plumes that correspond to the experimentally measured plumes in the rough-walled fracture in **Figure 5b**. For the simulations in **Figure 5c**, we used $\sim 3.5 \times 10^6$ particles (and adjusted the mass accordingly) to more closely approximate continuous concentration fields. Although the particle simulation fields are noisier, these images demonstrate excellent qualitative agreement of solute spreading between the simulations and experiments. The simulated solute plumes also exhibit slightly higher concentrations than the experimental plumes at the same locations. This is probably due to the underestimation of D_L by the simulations that is discussed in detail below. Note that increasing the number of particles by two orders of magnitude to generate **Figure 5c** resulted in less than a 1% change in estimated D_L. This indicates that we used a sufficient number of particles in our simulations to minimize variability in our estimates of D_L.

To quantitatively compare the results of the simulations to the experiments in both fractures, we plot D_L/D_m against Pe (**Figure 7**). As with simulations of flow in the Hele-Shaw cell [Nicholl et al., 1999], we expect that simulations of transport will agree closely with experimental results. Fitting (1b) to D_L/D_m measured from the simulations in the Hele-Shaw cell yields $\alpha_{Taylor}=(4.721\pm0.002) \times 10^{-3}$, which differs by less than 1% from the theoretical value of 4.762×10^{-3}. Dropping τ and fitting (5) to the simulation results in the rough-walled fracture yields estimates of $\alpha_{macro}=1.01\pm0.10$ and $\alpha_{Taylor}=(4.81\pm0.16) \times 10^{-3}$, which are 46% and 8% less than the experimentally measured values, respectively. Based on results presented by Detwiler et al. [1999] that investigated the influence of aperture measurement errors on estimates of α_{macro} from simulations, it is unlikely that these discrepancies are due to aperture measurement error. Underestimation of the magnitude of D_L is consistent with the inability of the Reynolds equation to fully describe the three-dimensional velocity field. Our simulations assume a local parabolic velocity profile across the aperture, but simulations of Stokes flow in two-dimensional variable aperture channels [e.g. Koplik et al., 1993; Brown et al., 1995; Gutfraind et al., 1995] have shown that velocity profiles are not uniformly parabolic throughout the channel.

Presumably, solving the three-dimensional Stokes equations will result in improved estimates of dispersion in the fracture. However, despite underestimating the magnitude of D_L, our simulations closely reproduce the functional dependence of D_L on Pe evident in the rough-walled fracture. We believe this is because over the Pe-range for which Stokes flow is valid, errors in the velocity field obtained by solving the Reynolds equation are proportional to the mean velocity (and hence Pe). Thus, in this range, estimates of D_L from simulations of transport should reliably reflect the actual Pe-dependence of D_L though they may underestimate the magnitude of D_L.

4.3. Computational simulations investigating the influence of σ_β^2 and λ over a wide range of Pe

Though the experiments and simulations in the rough-walled fracture both demonstrate the influence of Taylor dispersion on D_L, neither reach the Pe-range where macrodispersion becomes negligible (i.e. $D_L \propto Pe^2$) as predicted by the theory presented in Section 2. Additionally, our experimental aperture field embodies a single σ_β^2 and λ. In this section, we use numerical simulations to investigate the role of aperture variability (i.e. σ_β^2 and λ) over a wider Pe-range than was possible experimentally.

As discussed in Section 2, simulations at large values of Pe require fractures that are somewhat longer than 0.4<b>Pe (the distance required for Taylor dispersion to become fully developed). To investigate the influence of aperture variability (quantified by <b>, σ_β^2, and λ) on dispersion over a wide range of Pe, we generated three correlated random aperture fields that were significantly longer (7.9 cm x 169.9 cm, 512 x 11000 grid) than the experimental field: Field 1 with statistics (i.e.,<b>, σ_β^2, and λ) similar to those of the experimental field and Fields 2 and 3, with different values of λ and σ_β^2, respectively (**Table 4**). These longer fields satisfy the conditions for the full development of dispersion and thus allow meaningful comparison of theoretical results to computational simulations over a wide Pe-range.

We generated lognormally distributed aperture fields with a "hole-type" covariance function that captured the negative correlation caused by the slight periodicity of the experimental field. The spectral density function corresponding to this covariance function is:

$$S_{\beta\beta}(\omega_x, \omega_y) = \frac{16\sigma_\beta^2 \omega^2 \lambda^4}{\pi^3} \exp\left[\frac{-4\lambda^2\omega^2}{\pi}\right] \qquad (13)$$

where ω_x and ω_y are the wave numbers in the x and y-directions, $\omega = \sqrt{\omega_x^2 + \omega_y^2}$, and λ is the integral scale of the corresponding correlation function.

We used a fast Fourier transform algorithm to obtain $\beta(x,y)$, a normally distributed, correlated random field. Using this field, we generated the three synthetic, lognormally-distributed, aperture fields (b(x,y)) with statistics presented in **Table 4**. **Figure 8** compares the aperture distributions of the three synthetic fields and the experimental field. Synthetic Field 1 has the same σ_b and <b> as the experimental field, but exhibits a slightly

higher peak and less spread than the experimental field, due to the positive skew and long tail of the lognormal distribution. Note that although σ_b is equal for the two fields, σ_β (and thus α_{macro}) is slightly different due to the different shapes of the two distributions. **Figure 4** shows the normalized semivariograms of Field 1 and the experimentally measured rough-walled fracture, demonstrating that Field 1 is stationary and isotropic and has approximately the same correlation scale as the experimental field. Field 2 is identical to Field 1, except that the length of the side of each grid block, and thus λ, was increased by a factor of 50. We generated Field 3 by scaling the same $\beta(x,y)$ field used to generate Field 1 to increase σ_β^2 by a factor of 7.7 (or $10\sigma_b^2$). All three fields include a negative correlation at separations of ~2λ to ~4.5λ, as in the experimental field.

We simulated transport in each of the three random fields in the range $1 \lesssim Pe \lesssim 5x10^4$. Note that Pe=5.0 x 10^4 corresponds to a Reynolds number ($Re = V\langle b\rangle/\nu$) of 31.8. Experimental data presented by Nicholl et al. [1999] suggest that inertial forces in a fracture similar to Field 1 will begin to influence flow in the range 1<Re<10. Thus, these simulations surpass the range in which Stokes flow is expected to be valid. As a result, the simulation results for Pe>2x10^4 should be interpreted with caution. For all the simulations in the three synthetic fields, we used line source initial conditions spanning only the middle 2.5 cm (~70λ) of the fracture. This guaranteed that no particles reached the lateral boundaries before D_L became fully developed. As expected, for simulations at higher velocities (larger Pe), the plume required greater travel distances for Taylor dispersion to become fully developed. At the largest values of Pe reported here (~5.0 x 10^4), dM_{2x}/dt reached a constant value at a distance of approximately 70 cm (40% of the length of the field or ~0.06<b>Pe).

Figure 9 shows $D_L/(V\langle b\rangle)$ plotted against Pe for simulations in each of the three synthetic aperture fields, together with theoretical results that will be discussed in detail in Section 5. At large Pe, all three sets of simulations illustrate the progressive dominance of Taylor dispersion, where $D_L \propto Pe^2$. However, simulations in each field exhibit markedly different behavior at intermediate values of Pe (i.e. $\sim 10^0 < Pe < 10^3$). The simulations in Field 2 (large λ) indicate $D_L \propto Pe$ over almost this entire intermediate range of Pe values, whereas the simulations in Field 1 indicate almost no range where $D_L \propto Pe$. Simulations in Field 3 (large σ_β^2) indicate $D_L \propto Pe$ in a Pe range that is between the corresponding Pe range in Fields 1 and 2. It is clear that as σ_β^2 and/or λ increase, there is a corresponding increase in the magnitude of α_{macro} and hence a larger range of Pe in which $D_L \propto Pe$.

5. Comparison of theory to physical experiments and computational simulations

The results of the transport simulations over the range $O(10^0)<Pe<O(10^5)$ (**Figure 9**) exhibit the three distinct dispersion regimes suggested by Roux et al. [1998]: molecular diffusion, Taylor dispersion, and macrodispersion. In this section, we compare the theoretical estimates of α_{macro} and α_{Taylor} obtained from (1b) and (2b) to estimates from the experimental and computational results.

To calculate the theoretical estimates of α_{macro} for the experimental rough-walled fracture and the three synthetic fields, we applied (2b) to estimates of $I(\sigma_\beta^2)$ calculated for each field by numerically integrating the corresponding covariance function. **Figure 10** shows D_L/D_m plotted against Pe for the experimental field (experimental, computational and theoretical results) and Field 1 (computational and theoretical results). For Field 1, theoretical and computational results are almost identical, with a discrepancy of < 1% at Pe=300. This indicates that (2b) and (5) are accurate in a variable aperture fracture, when the underlying assumptions (local cubic law flow, a stationary, lognormally-distributed, aperture field, and small σ_β) are satisfied, as is the case for the simulations in Field 1. The theoretical estimates of D_L/D_m for the experimental fracture are smaller (by ~ 9% at Pe=300) than the estimates from the computational results (**Figure 10**). This discrepancy, which is larger than that observed for Field 1, is likely because the aperture field is not lognormally distributed, as this is the primary discrepancy between the assumptions of the theory and the computational simulations in this field. Another possible reason may be that the simulations were carried out in one realization, whereas the theory predicts ensemble average behavior. However, the relatively large source width (~28λ) for our single realizations leads us to expect closer agreement with the ensemble average theory. The experimental results for D_L/D_m in the experimental field are substantially larger than the theoretical estimates (by ~ 51% at Pe=300). Of this 51% discrepancy, about 9% can be explained by the deviation between the computational and theoretical results just noted. Thus, by process of elimination, the remaining portion of the discrepancy between theoretical and experimental values (~42%) reflects the influence of deviations from the Reynolds equation in the flow field.

The theoretical value of α_{Taylor} (2a) for each field is 4.76×10^{-3}. This value is 9% smaller than that obtained by fitting (5) to the experimental results and 1% less than that obtained from the simulations (Table 3). The small discrepancy between the theoretical α_{Taylor} and the value estimated from simulations indicates that calculating an effective $D_{L,Taylor}$ based on the mean aperture and flow velocity provides a good estimate of the influence of Taylor dispersion in the rough-walled fracture. The small discrepancy between the experimentally measured α_{Taylor} and the theoretical value indicate that deviations from the Reynolds equation do not influence α_{Taylor} as much as they influence α_{macro}.

Figure 9 shows $D_L/(V<b>)$ plotted against Pe for both theoretical and computational results for Fields 1, 2 and 3. There is excellent agreement between the theoretical results and simulations because both employ the Reynolds equation to describe flow through a rough-walled fracture. Also, the aperture fields are lognormally distributed, as assumed in the derivation of the theoretical results. Even though the simulations were carried out in a single realization, the good agreement with the ensemble average theory is

probably due to the large source sizes (~70λ) transverse to the mean flow. It may also be noted that the agreement between simulations and theory is poorer in Field 3 than in Fields 1 and 2. This is likely because σ_β^2 is larger for Field 3 and there is an assumption of small σ_β^2 implicit in the theoretical results.

In summary, comparing theoretical results to experimental and computational results demonstrated the following:
i) excellent agreement between theory and simulations in synthetic, lognormal, random fields, due to the consistency of the assumptions (i.e., both are based on the Reynolds equation);
ii)small discrepancies between simulations and theory for the rough-walled experimental fracture, likely due to the assumption of a lognormal aperture distribution implicit in the theory;
iii) poorer agreement between theoretical and experimental results, highlighting the additional influence of deviations of the actual velocity field from that described by the Reynolds equation, on estimates of D_L;
iv) good agreement between theoretical and experimental/computational estimates of α_{Taylor} indicating that the "effective" Taylor dispersion coefficient defined by $V^2<b>^2/(210D_m)$ is a good estimate of the influence of Taylor dispersion in a variable aperture fracture;
v) good agreement between theory and numerical simulations for fields with different σ_β^2 and λ, indicating that when the assumptions of the Reynolds equation are met, equation (6) effectively characterizes the Pe regimes where different dispersion mechanisms dominate.

6. Concluding remarks

We have described a series of physical and computational transport experiments designed to clarify the Peclet number (Pe) dependence of the longitudinal dispersion coefficient (D_L) in a saturated, variable-aperture fracture. During physical experiments in two analog glass fractures (a parallel plate fracture (Hele Shaw cell) and a rough-walled fracture), aperture and concentration fields were measured using an accurate light transmission technique. Computational simulations in the measured aperture fields were compared to experimental results and the role of aperture variability on the Pe-dependence of D_L was investigated through additional simulations in three synthetically generated random aperture fields. The flow fields for the transport simulations were generated by solving the Reynolds equation in each aperture field. The three-dimensional velocity fields within the fractures incorporated parabolic velocity profiles across the aperture, with magnitudes based on the local aperture-averaged velocity obtained from the Reynolds equation solution. A three-dimensional particle-tracking algorithm was then used to simulate solute transport. This approach enabled us to represent the influence of both macrodispersion and Taylor dispersion, in contrast to previous approaches, which have isolated one or the other of these mechanisms.

Excellent agreement between simulations and experiments in the Hele-Shaw cell verified our computational model under simple conditions. In the rough-walled fracture, both physical and computational experiments demonstrated a nonlinear relationship between D_L and Pe. In particular, our results confirmed two of the distinct dispersion regimes suggested by Roux et al. [1998]. At intermediate values of Pe, macrodispersion dominated ($D_L \propto Pe$) and at large Pe values, Taylor dispersion dominated ($D_L \propto Pe^2$). We predicted D_L throughout this range using a simple theoretical model that represents the total longitudinal dispersion coefficient as the sum of a macrodispersion coefficient based on the stochastic analysis of Gelhar [1987,1993] and a Taylor dispersion coefficient based on the mean solute velocity and the mean aperture. This theoretical model, which also incorporates the assumptions inherent in the Reynolds equation, agreed closely with simulations in synthetic, lognormally-distributed, aperture fields. However, though the theoretical model and numerical simulations captured the Pe-dependence of D_L in the experimental fracture quite well, they underestimated the magnitude of D_L. We demonstrated, by process of elimination, that this discrepancy is primarily due to inadequacies of the Reynolds equation. Thus, the ability of the theoretical model to describe dispersion will be closely tied to the validity of the Reynolds equation in a given fracture.

The theoretical model shows that the statistics of the aperture field determine the specific nature of the Pe-dependence of D_L. In particular, the Pe-ranges in which different dispersion mechanisms dominate vary with aperture statistics ($\langle b \rangle$, σ_β^2, and λ). The theoretical model assumes that the aperture field can be described as a stationary lognormal random field. Brown [1995] suggested that when two rough surfaces are brought together to form a fracture, there is a length scale (mismatch length scale) above which aperture variability is essentially stationary due to correlation between the two surfaces. Thus, although studies of fracture surfaces have demonstrated variability in topography over multiple length scales [e.g., Brown and Scholz, 1985; Poon et al., 1992; Schmittbuhl et al., 1993; Plouraboue et al., 1995; Power and Tullis, 1995], the largest being of the order of the sample size (up to O(1) m), the aperture field formed by two of these surfaces may not exhibit the same multi-scale characteristics. This hypothesis is supported by a number of measurements made of natural fractures (see Table 5) but is clearly an area that merits more study. Our analog, rough-walled fracture was statistically homogeneous, with mean and variance within the range measured in these actual fractures. Additionally, the

correlation scale λ_e, (defined here as the separation distance at which the semivariogram reaches a value = (1-1/e) times the sill value, which is identical to the integral scale in the case of an exponential covariance function) was much smaller than the dimensions of the fracture. This avoided the influence of channeling at scales of the order of the sample size, thus allowing meaningful comparison to theoretical results.

For the previously published aperture statistics for fractures in rock samples detailed in Table 5, we calculated the Pe value (Pe = 210 α_{macro}) at which the Taylor dispersion and macrodispersion coefficients are equal (column 7 in Table 5). The values of B used for calculating α_{macro} (2b) assumed an exponential covariance function; note that the exact shape of the covariance function has only a mild influence on B, through the integral in (4). The corresponding Reynolds number (Re) (column 8 in Table 5) clarifies whether the high velocities associated with macrodispersion/Taylor dispersion equivalence are within the "Darcian" region (i.e. linear relation between the mean hydraulic gradient and the mean flux). Values of Re > ~1-10 imply that rather than the Taylor dispersion regime, a new dispersion regime is likely, where dispersion will be influenced by non-Darcian flow effects resulting from the inertial terms in the Navier-Stokes equations. We see that in the limestone, granite and welded tuff fractures characterized by Kumar et al. [1995], Yeo et al. [1998], and Wan et al. [in press], respectively, the influence of Taylor dispersion will be evident (for solute transport in water) at $Re \leq 1.0$. Thus, there is a range of flow rates for these fractures in which Taylor dispersion will be the dominant dispersion mechanism, just as we have found in our analog, rough-walled fracture. For the granite fractures measured by Hakami and Larsson [1996] and Keller et al. [1999], the value of Pe at which Taylor dispersion will begin to dominate, corresponds to $1 < Re < 10$. In these fractures, though Taylor dispersion may not become the dominant dispersion mechanism before the flow becomes non-Darcian, the influence of Taylor dispersion will result in a nonlinear relationship between Pe and D_L at high flow rates.

The occurrence of both macrodispersion and Taylor dispersion regimes in fractures can have significant implications on interpreting tracer tests at the single-fracture scale. For instance, in radial flow tracer tests, the mean flow velocity increases as solute approaches the well. As a result, macrodispersion can be the dominant dispersion mechanism far from the well, whereas Taylor dispersion effects become increasingly important close to the well. Commonly used interpretation techniques [e.g., Raven et al., 1988; Maloziewski and Zuber, 1990; Cady et al., 1993; Novakowski et al., 1995] incorporate only a dispersion coefficient that is a linear function of velocity, implicitly assuming that Taylor dispersion effects are insignificant. The analysis of Hodgkinson and Lever [1983], on the other hand, incorporates only Taylor dispersion. Subtle nonlinear Pe-dependence of D_L may also be important, when using multiple tracers with widely differing molecular diffusion coefficients. The Pe values corresponding to the different tracers under the same hydraulic conditions can vary over 1-2 orders of magnitude, placing the different tracers in different dispersion regimes. The Pe-dependence of D_L, however, is typically ignored in interpreting these tracer tests [e.g., Maloziewski and Zuber, 1990].

Another important feature that merits additional study is the fundamental difference between the Pe-dependence of D_L in variable aperture fractures and porous media. Several studies in porous media indicate a linear relationship between D_L and Pe at high Pe ($Pe > 10^3$) [e.g., Fried and Combarnous, 1971]. This linear relationship breaks down only when the Pe value becomes so large that the flow becomes non-Darcian. We believe that this feature relates to the difference in the topology of the void space in fractures and porous media. In most fractures used in previously reported experiments and in our study, the fraction of contact area between the fracture surfaces is relatively small. The resulting long,

simply-connected flow paths permit Taylor dispersion to "develop". However, due to the complex tortuous topology of the pore space in porous media there may not be an opportunity for Taylor dispersion to develop, especially at high Pe, where the travel time through a single pore throat will be very small [e.g. Bear, 1972]. Additional computational and experimental studies in fractures with larger fractions of contact area and in porous media, would help to clarify the fundamental reasons for the difference of the Pe-dependence of D_L between fractures and porous media.

Appendix: Influence of concentration measurement errors on estimates of D_L

As with light transmission measurements of aperture fields, concentration field measurements are subject to random errors due to CCD image noise and accuracy or systematic errors (e.g., nonlinear dye absorbance, reflections and refraction). Unlike aperture measurements, concentration measurements can be easily calibrated by sequentially filling the fracture with standards of known concentration and fitting (9) to the measurements at each pixel. Calibration effectively minimizes accuracy errors leaving image noise as the primary error source. The influence of noise can be quantified by measuring the difference between the actual concentration in the fracture during calibration and the concentration calculated using the calibration curves developed at each pixel. Averaging the difference between the measured concentration at each pixel and the actual concentration over the entire field, yielded a maximum mean error $0.003C_o$ ($C_o = 0.25$ g/l). This indicates that (9) fits the data well and that errors are predominantly due to random signal noise. The root-mean-square (RMS) errors at individual pixels ranged from $0.001C_o$ for the 0 g/l fields in both fractures to $0.023C_o$ and $0.019C_o$ for the 0.25 g/l field in the Hele-Shaw cell and the rough-walled fracture, respectively. These random errors do not influence our estimates of D_L because in calculating D_L, we combine measurements from thousands of pixels which significantly reduces the influence of noise.

Despite calibrating our measurement system, the reflective coating on the surface of the band-pass-filter on the camera lens caused additional errors in our concentration measurements when the fracture was not filled entirely with one concentration (i.e., during solute transport experiments). These errors included an artificial, reflected plume that was ~1% of the concentration of the real plume and led the real plume through the fracture by ~7.1 cm. We also observed a trend in background concentrations in some fields that resulted in additional mean errors ranging from $0.003C_o$ at the inflow end of the fracture to ~ $-0.003C_o$ at the outflow end of the fracture. This trend in background concentrations may be due to a small shift in the intensity of the light source that was not uniform over the entire field. Because the background trend remained relatively constant over the several days that we performed the experiments, this shift appears to be a one time occurrence after we obtained the calibration images and before we ran the experiments. Because these two additional sources of concentration measurement error were consistent from image to image, we were able to develop an image processing algorithm to minimize the influence of these errors on estimates of dispersion coefficients.

To remove our observational bias and to streamline the processing of over 700 experimental images, we developed a processing routine that consisted of four primary steps (described in detail below): 1) subtract the reflected plume from each image, 2) apply a median filter to the entire concentration field, 3) define a region of interest (ROI) that completely surrounds the plume but excludes small errors far from the plume and 4) apply a thresholding routine inside the ROI to isolate the plume from any trend in background concentrations within the ROI. We varied the parameters used in this routine to bound the possible values of D_L measured for each experiment. These bounds are displayed as error bars in **Figure 6**. Note that the error bars represent the possible range of values of D_L not a standard deviation or confidence interval.

We removed the reflected plume from each image by scaling and shifting the real plume appropriately and subtracting it from the concentration field. Using a median filter, which sets the value at each pixel to the median value of a 5 x 5 pixel box surrounding the pixel, we reduced noise and any anomalous measurements from the field. This filtering step smoothed the concentration field slightly, but since the resolution of our measurements

(pixel size = 0.0154 x 0.154 cm) was significantly smaller than the scale of real concentration variations within the field, the effect of this smoothing on our estimates of D_L was negligible. We then defined a small ROI centered at the first moment of the real plume and, using (12), measured the second spatial moment of the ROI. Incrementally increasing the size of this ROI resulted in a plot of second moment versus ROI size which at first grew quickly and then leveled off. The degree to which the slopes of plots of M_2 versus ROI size leveled off depended on the magnitude and relative location of the trend in the background concentrations. However, for each experimental image, the value of M_2 at which the slope first began to level off ($M_{2_{est}}$) was directly related to the size of the plume. We defined an ROI around the plume that had a width and height of $8\sqrt{M_{2_{est}}}$ as we found a region of this size captured the entire plume and a buffer around the plume (this corresponds to the size of the third frame shown in **Figure 5b**). We then obtained the worst case overestimation of D_L by measuring M_2 of this entire ROI. We defined a threshold concentration equal to 0.3% of the maximum mass measured in the solute plume from the initial image of each series. By setting all values within the ROI that were less than this threshold to zero, we obtained the worst case underestimation of D_L. We obtained the best estimation of D_L by dilating the region defined by the thresholding routine to include pixels with low mass in the vicinity (~8 pixels) of the plume that were below the threshold concentration.

Acknowledgments

This work was supported by the U.S. Department of Energy's Basic Energy Sciences Geoscience Research Program under contract numbers DE-FG03-96ER14590 (University of Colorado at Boulder) and DE-AC04-94AL85000 (Sandia National Laboratories). We thank Brian Bloechle, Sean McKenna and two anonymous reviewers for their constructive reviews of the manuscript. Experiments were conducted at the Flow Visualization and Processes Laboratory at Sandia National Laboratories.

References

Aris, R., On dispersion of a solute in a fluid flowing through a tube, *Proc. R. Soc. Lond.*, A235, 66-77, 1956.

Bear, J., *Dynaimcs of fluids in porous media.* New York: Dover Publishing, 1972.

Brown, S.R. and C.H. Scholz, Broad bandwidth study of the topography of natural rock surfaces, *J. Geophys. Res.*, 90(B14), 12,575-12,582, 1985.

Brown, S.R., A simple mathematical model of a rough fracture, *J. Geophys. Res.*, 100(B4), 5941-5952, 1995.

Brown, S.R., H.W. Stockman, and S.J. Reeves, Applicability of the Reynolds equation for modeling fluid flow between rough surfaces, *Geophys. Res. Lett.*, 22, 2537-2540, 1995.

Cady, C.C., S.E. Silliman, and E. Saffern, Variation in aperture estimate ratios from hydraulic and tracer tests in a single fracture, *Water Resour. Res.*, 29(9), 2975-2982, 1993.

Cussler, E.L., *Diffusion, mass transfer in fluid systems.* Cambridge: Cambridge University Press, 1984.

Dagan, G., Solute transport in heterogeneous porous formations, *J. Fluid Mech.*, 145, 151-177, 1984.

Detwiler, R.L., S.E. Pringle, and R.J. Glass, Measurement of fracture aperture fields using transmitted light: An evaluation of measurement errors and their influence on simulations of flow and transport through a single fracture, *Water Resour. Res.*, 35(9), 2605-2617, 1999.

Doshi, M.R., M.D. Daiya, and W.N. Gill, Three dimensional laminar dispersion in open and closed rectangular conduits, Chemical Engineering Sciences, 33, 795-804, 1978.

Dronfield, D.G. and S.E. Silliman, Velocity dependence of dispersion for transport through a single fracture of variable roughness, *Water Resour. Res.*, 29(10), 3477-3483, 1993.

Fischer, H.B., E.J. List, R.C.Y. Koh, J. Imberger, and N.H. Brooks, *Mixing in inland and coastal waters.* San Diego: Academic Press, 1979.

Fried, J.J. and M.A. Combarnous, Dispersion in porous media, *Advances in Hydroscience*, 7, 170-282, 1971.

Gelhar, L.W., Applications of stochastic models to solute transport in fractured rocks, Swedish Nuclear Fuel and Waste Management Co., 1987

Gelhar, L.W., *Stochastic subsurface hydrology*: Englewood Cliffs, New Jersey, Prentice-Hall, Inc. 1993.

Glass, R.J., M.J. Nicholl, and M.E. Thompson, Comparison of measured and calculated permeability for a saturated, rough-walled fracture, *EOS*, 72(44), 216, 1991.

Gutfraind, R., I. Ippolito, and A. Hansen, Study of tracer dispersion in self-affine fractures using lattice-gas automata, *Phys,* Fluids, 7(8), 1938-1948, 1995.

Hakami, E. and E. Larsson, Aperture measurements and flow experiments on a single natural fracture, *International Journal of Rock Mechanics and Mining Sciences & Geomechanics Abstracts*, 33 , 395-404, 1996.

Hodgkinson, D.P. and D.A. Lever, Interpretation of a field experiment on the transport of sorbed and non-sorbed tracers through a fracture in crystalline rock, *Radioactive Waste Management and the Nuclear Fuel Cycle*, 4(2), 129-158, 1983.

Hull, L.C., J.D. Miller, and T.M. Clemo, Laboratory and simulation studies of solute transport in fracture networks, *Water Resour. Res.*, 23, 8, 55-63, 1987.

Ippolito, I., G. Daccord, E.J. Hinch, and J.P. Hulin, Echo tracer dispersion in model fractures with a rectangular geometry, *Journal of Contaminant Hydrology*, 16, 87-108, 1994.

Keller, A.A., P.V. Roberts, and P.K. Kitankdis, Prediction of single phase transport parameters in a variable aperture fracture, *Geophys. Res. Lett.*, 22, 1425-1428, 1995.

Keller, A.A., P.V. Roberts, and M.J. Blunt, Effect of fracture aperture variations on the dispersion of contaminants, *Water Resour. Res.*, 35, 1, 55-63, 1999.

Koplik, J., I. Ippolito, and J.P. Hulin, Tracer dispersion in rough channels: A two dimensional numerical study, *Phys. Fluids A*, 5(6), 1333-1343, 1993.

Kumar, A.T.A., P.D. Majors, and W.R. Rossen, Measurement of Aperture and Multiphase Flow in Fractures using NMR Imaging, *Proc. SPE Annual Technical Conference and Exhibition*, 279-290, 1995.

Malozewski, P. and A. Zuber, Mathematical modeling of tracer behavior in short-term experiments in fissured rocks, *Water Resour. Res.*, 26(7), 1517-1528, 1990.

Moreno, L., Y.W. Tsang, C.F. Tsang, F.V. Hale, and I. Neretnieks, Flow and tracer transport in a single fracture: a stochastic model and its relation to some field observations, *Water Resour. Res.*, 24(12), 2033-2048, 1988.

Nicholl, M.J., H. Rajaram, R.J. Glass, and R.L. Detwiler, Saturated flow in a single fracture: evaluation of the Reynolds equation in measured aperture fields, *Water Resour. Res.*, 1999.

Novakowski, K.S., P.A. Lapcevic, J. Voralek, and G. Bickertion, Preliminary interpretation of tracer experiments conducted in a discrete rock fracture under conditions of natural flow, *Geophys. Res. Lett.*, 22(11) 1417-1420, 1995.

Plouraboue, F., P. Kurowski, J.P. Hulin, S. Roux, and J. Schmittbuhl, Aperture of rough cracks, *Phys. Rev. E*, 51(3), 1675-1685, 1995.

Poon, C.Y., R.S. Sayles, and T.A. Jones, Surface measurement and fractal characterization of naturally fracture rocks, *J. Phys. D: App. Phys.* 25, 1269-1275, 1992.

Power, W.L. and T.E. Tullis, Review of the fractal character of natural fault surfaces with implications for friction and the evolution of fault zones, Fractals in the Earth Sciences, Barton, C. C. and P. R. La Pointe (editors), Plenum Press; New York, 89-105, 1995.

Raven, K.G., K.S. Novakowski, and P.A. Lapcevic, Interpretation of field tracer tests of a single fracture using a transient solute storage model, *Water Resour. Res.*, 24, 2019-2032, 1988.

Reejhsinghani, N.S., W.N. Gill, and A.J. Barduhn, Part III. Experiments in horizontal tubes including observations on natural convection effects, A.I.Ch.E. Journal, 12, 916-921, 1966.

Roux, S., F. Plouraboue, and J. P. Hulin, Tracer dispersion in rough open cracks, *Transport in Porous Media*, 32, 97-116, 1998.

Schmittbuhl, J., S. Gentier, and S. Roux, Field measurements of the roughness of fault surfaces, *Geophys. Res. Lett.*, 20(8), 639-641, 1993.

Stockman, H.W., A lattice gas study of retardation and dispersion in fractures: Assessment of errors from desorption kinetics and buoyancy, *Water Resour. Res.*, 33(8), 1823-1831, 1997.

Taylor, G., Dispersion of soluble matter in solvent flowing slowly through a tube, *Proceedings of the Royal Society*, 219A, 186-203, 1953.

Thompson, M.E., Numerical simulation of solute transport in rough fractures, *J. Geophys. Res.*, 96(B3), 4157-4166, 1991.

Thompson, M.E. and S.R. Brown, The effect of anisotropic surface roughness on flow and transport in fractures, *J. Geophys. Res.*, 96(B13), 21,923-21,932, 1991.

Wan, J., T.K. Tokunaga, J. O'Neill, and R.O. Thomas, Glass casts of rock fracture surfaces: A new tool for studying flow and transport, *Water Resour. Res.*, in press.

Yeo, I.W., M.H. De Freitas, and R.W. Zimmerman, Effect of shear displacement on the aperture and permeability of a rock fracture, *Int. J. Rock Mech. Min. Sci.*, 35(8), 1051-1070, 1998.

Zimmerman, R.W., and G.S. Bodvarsson, Hydraulic conductivity of rock fractures, *Transport in Porous Media*, 23, 1-30, 1996.

Table 1: Fracture dimensions and measured aperture statistics

	Hele-Shaw	rough-walled
Dimensions (cm x cm)	15.3 x 30.5	14.8 x 30.2
Dimensions (pixels x pixels)	972 x 1940	958 x1958
Dimensions (λs x λs)	--	336 x 686
Pixel size (cm)	1.57×10^{-2}	1.54×10^{-2}
Minimum aperture (cm)	1.72×10^{-2}	1.30×10^{-3}
Maximum aperture (cm)	2.09×10^{-2}	3.85×10^{-2}
<b> (cm)	1.93×10^{-2}	2.21×10^{-2}
σ_β (cm)	5.27×10^{-4}	6.02×10^{-3}
σ_β/<b>	2.73×10^{-2}	2.72×10^{-1}
λ - long axis (cm) *	--	4.4×10^{-2}
λ - short axis (cm) *	--	4.4×10^{-2}
RMS Error (% of mean)	0.8	1.2

* - In this study λ represents the integral scale calculated by numerically integrating $\int_{r=0}^{r=\max} \rho(r)dr$, where $\rho(r) = 1 - \gamma(r)/\sigma_b^2$ is the correlation function and $\gamma(r)$ is the semivariogram. Previous studies using similar fractures [e.g., Glass et al., 1998; Nicholl et al., in review] measured λ as the separation length at which the semivariogram reached the level of the sill (~0.08 cm).

Table 2: Summary of experiments and results

Fracture	Experiment	Measured Flow Rate (cm^3/s)	Mean Velocity (cm/s)	Reynolds Number	Peclet Number	D_L (cm^2/s)
Hele-Shaw Cell	1	0.0121	0.043	0.08	147.39	6.26×10^{-04}
	2	0.0220	0.077	0.15	264.23	2.01×10^{-03}
	3	0.0288	0.100	0.19	343.02	3.27×10^{-03}
	4	0.0348	0.121	0.24	414.77	4.78×10^{-03}
	5a	0.0421	0.146	0.28	500.41	6.96×10^{-03}
	5b	0.0419	0.146	0.28	500.60	7.05×10^{-03}
	5c	0.0417	0.145	0.28	499.41	7.10×10^{-03}
	6	0.0494	0.171	0.33	588.73	9.56×10^{-03}
	7	0.0571	0.199	0.39	682.35	1.28×10^{-02}
	8	0.0617	0.214	0.42	736.83	1.48×10^{-02}
Rough-walled Fracture	1	0.0114	0.037	0.08	142.63	2.08×10^{-03}
	2	0.0147	0.048	0.11	185.50	2.87×10^{-03}
	3	0.0190	0.060	0.13	235.55	4.06×10^{-03}
	4	0.0287	0.090	0.20	352.03	7.80×10^{-03}
	5a	0.0340	0.108	0.24	421.49	9.59×10^{-03}
	5b	0.0340	0.108	0.24	419.04	9.52×10^{-03}
	5c	0.0338	0.107	0.24	418.60	9.59×10^{-03}
	6	0.0403	0.128	0.28	497.77	1.26×10^{-02}
	7	0.0467	0.147	0.32	572.09	1.60×10^{-02}
	8	0.0534	0.168	0.37	656.27	1.98×10^{-02}
	9	0.0612	0.193	0.43	751.21	2.46×10^{-02}

Table 3: Fitted values of α_{macro} and α_{Taylor} for experiments and simulations and theoretical values based on (2a) and (2b)

		α_{macro}	α_{Taylor}
Hele-Shaw			
	Experiments	na	0.00476 +/- 0.00004
	Simulations	na	0.00472 +/- 0.00002
	Theory	na	0.00476
Rough-wall			
	Experiments	1.87 +/- 0.15	0.00522 +/- 0.00026
	Simulations	1.01 +/- 0.10	0.00481 +/- 0.00016
	Theory	0.77	0.00476
Field-1			
	Simulations	0.41 +/- 0.20	0.00472 +/- 0.00033
	Theory	0.47	0.00476

na - Not applicable
Note, tolerances are 95% confidence intervals for the fitted parameters.

Table 4: Comparison of statistics and macrodispersivity for synthetic and experimental aperture fields

Aperture Field	$\langle b \rangle$ (cm)	σ_b (cm)	σ_β^2	λ (cm)	$^*I(\sigma_\beta^2)/\sigma_\beta^2$	α_{macro}
Field-1	0.022	0.0060	0.073	0.035	1.04	0.47
Field-2	0.022	0.0060	0.073	1.8	1.04	23
Field-3	0.022	0.019	0.56	0.035	1.32	3.9
Experimental	0.022	0.0060	0.096	0.044	1.05	0.78

* - For the aperture fields used in this study, $R_{\beta\beta}(s) = \sigma_\beta^2\left(1-\frac{\pi r^2}{16\lambda^2}\right)\exp\left[-\frac{\pi r^2}{16\lambda^2}\right]$ was used to derive these values.

Table 5: Comparison of aperture field statistics

	Fracture Type	<b> (cm)	σ_b (cm)	σ_β^2	λ_e*** (cm)	Pe=210α_{macro} ◊	Re ◊◊
Brown [1995] ****	Variety	--	0.0017-0.018	--	0.065-1.5	--	
Kumar et al. [1995]	Limestone	0.027	0.0051	0.036 *	0.3	340	0.51
Keller et al. [1995]	Granite	0.038	--	0.18 **	4	16000	24
Hakami and Larson [1996]	Granite	0.036	0.015	0.16 *	0.3	1100	1.7
Keller et al. [1999]	Granite	0.083	0.068	0.24 **	0.6	1500	2.2
Yeo et al. [1998]	Granite	0.0607	0.0160	0.067 *	<0.5	460	0.7
Wan et al. [in press] *****	Tuff	0.0281	0.0088	0.114	0.2	690	1.0
Rough-walled fracture (current study)	Analog	0.0221	0.006	0.073	0.05	140	0.2

* - Based on reported values of σ_b assuming a lognormal aperture distribution.

** - Estimated based on the reported value of σ_{lnT}^2.

*** - Estimated integral scale of the log aperture field; based on the approximate separation at which the semivariogram reaches a level of $\sigma^2(1-1/e)$.

**** - Based on numerically combining measurements of individual surfaces.

***** - Reported values for 0 displacement between fracture surfaces.

***** - Based on light transmission measurements made in the Flow Visualization and Processes Laboratory, Sandia National Laboratories.

◊ - 210α_{macro} is the value of Pe at which Taylor dispersion equals macrodispersion.

◊◊ - Reynolds number corresponding to Pe= 210α_{macro} assuming D_m=1.5 x 10^{-5} cm^2/s (typical for commonly used ionic tracers) and ν=1.0 x 10^{-2} cm^2/s.

-- - Not available.

Figure Captions

Figure 1. Theoretical D_L/D_m versus Pe for α_{macro}=0.2 and 20, τ=1, and α_{Taylor}=1/210. For α_{macro}=0.2, D_L/D_m transitions directly from the molecular diffusion regime (slope=0) to the Taylor dispersion regime (slope=2), whereas for larger α_{macro} the macrodispersion regime (slope=1) becomes a distinct third regime.

Figure 2. Theoretical $D_L/(V<b>)$ versus Pe for α_{macro}=0.2 and 20. This method of nondimensionalizing D_L highlights the three different dispersive regimes: molecular diffusion (slope=-1), macrodispersion (slope=0), and Taylor dispersion (slope=1).

Figure 3. **(a)** Schematic plan view of fracture cell and plumbing layout, **(b)** Cross-section view of Hele-Shaw cell and **(c)** Cross-section view of rough-walled fracture.

Figure 4. Semivariograms (γ) of the two experimental fractures and synthetic Field-1. The semivariogram for the rough-walled fracture demonstrates the stationary, isotropic nature of the aperture field. The semivariogram for the Hele-Shaw cell indicates a relatively strong trend across the width of the cell and a milder trend along the length of the cell. The semivariogram for Field-1 is very similar to the rough-walled fracture demonstrating the similarity between the correlation structure of the synthetic and experimental field.

Figure 5. A portion of three concentration fields measured during (a) an experiment in the Hele-Shaw cell, (b) an experiment in the rough-walled fracture, and (c) a simulation in the rough-walled fracture. Each field represents a 3 cm x 9 cm region of the fracture centered on the first spatial moment of solute mass in the x-direction and the center of the fracture in the y-direction. In the Hele-Shaw cell, M_{1x}= 1.1, 6.6, and 12.0 cm in the three frames and in the rough-walled fracture, M_{1x}= 1.6, 5.4, and 9.4 cm in the three frames. In the Hele-Shaw cell, the effect of Taylor dispersion is evident as growth of the plume in the flow direction with little spreading perpendicular to the flow direction. In the rough-walled fracture, the enhanced dispersion caused by aperture variability is evident.

Figure 6. Nondimensional dispersion coefficient (D_L/D_m) plotted against the Peclet number (Pe) for experiments in both fractures. The curves through the data points are the result of fitting (5) to the data. **Table 3** lists the fitted parameters for the rough-walled fracture. The error bars represent the possible range of D_L estimates resulting from concentration measurement errors (see the Appendix for a discussion of errors).

Figure 7. Comparison of D_L/D_m versus Pe for experiments and simulations in the Hele-Shaw cell and the rough-walled fracture. The curves through the Hele-Shaw cell data represent (1b), the theoretical expression for Taylor dispersion. The curves through the data represent (5) fitted to each data set (neglecting τ). The fitted parameters are presented in **Table 3**.

Figure 8. Comparison of aperture distributions for experimental fracture and the three synthetic fields (Fields 1, 2, and 3). Synthetic Fields 1 and 2 have the same variance as the experimental field. The synthetic fields exhibit a positive skew due to the lognormal distribution and the experimental field exhibits a negative skew. Field-3 has a larger variance and the same mean as the other fields resulting in a higher percentage of small aperture values.

Figure 9. Results of simulations (data points) and theoretical expressions (lines) in Fields 1, 2, and 3. The theory predicts identical small and large Pe behavior for all three fields, but at intermediate values of Pe where macrodispersion dominates, the influence of σ_β^2 and λ on the magnitude of macrodispersion are evident. The simulations agree closely with theory for Fields 1 and 2; deviations for Field 3 are likely due to the increase in σ_β^2 (the theory assumes small σ_β^2).

Figure 10. Comparison of theoretical results for the rough-walled fracture and synthetic Field 1 to experimental and computational results. The close agreement between theory and simulations in both fields indicates that when the assumptions of the Reynolds equation are valid for a given fracture, the theoretical expression described by (5) provides a good estimate of the total dispersion coefficient.

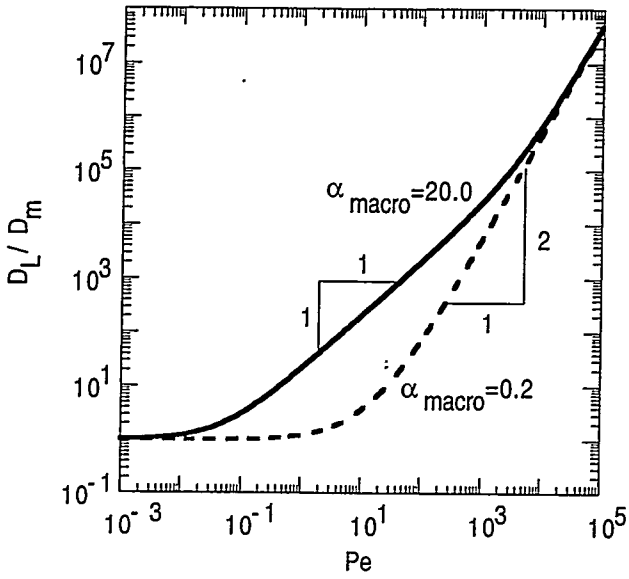
10^7
10^5
10^3
10^1
10^{-1}
D_L / D_m
α_{macro}=20.0
α_{macro}=0.2
1
1
2
1
10^{-3}
10^{-1}
10^1
10^3
10^5
Pe

Figure 1

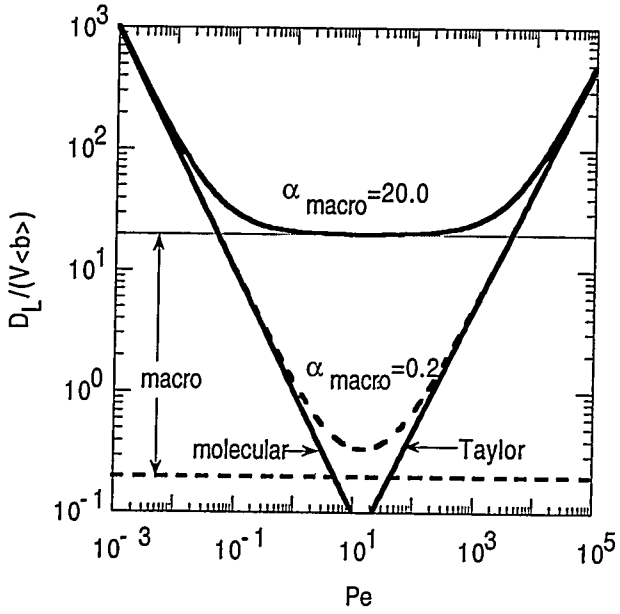
10^3
10^2
10^1
10^0
10^{-1}
$D_L/(V<b>)$
α_{macro}=20.0
α_{macro}=0.2
macro
molecular
Taylor
10^{-3}
10^{-1}
10^1
10^3
10^5
Pe

Figure 2

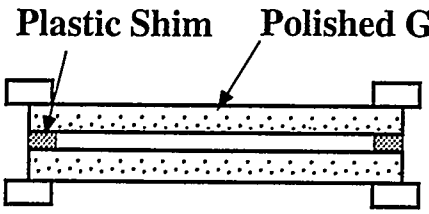

Cross-Section X-X'
Hele-Shaw cell

Figure 3b

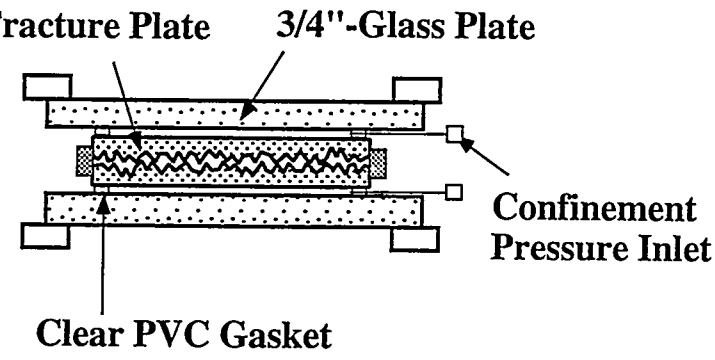

Cross-Section X-X'
Rough-walled fracture

Figure 3c

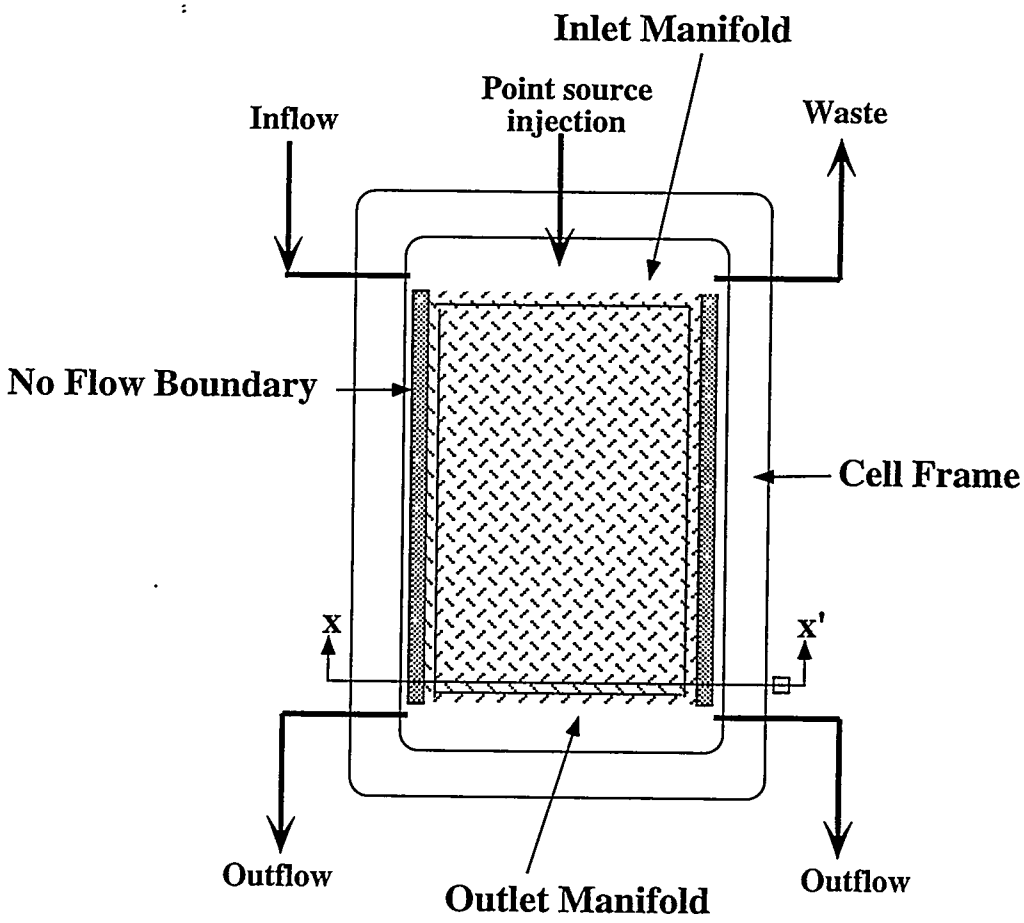

Plan View

Figure 3a

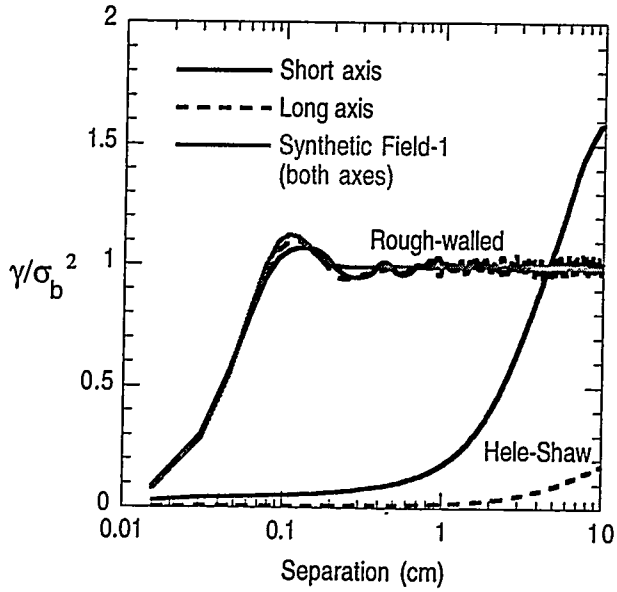
2
1.5
1
0.5
0
γ/σ_b^2
Short axis
Long axis
Synthetic Field-1
(both axes)
Rough-walled
Hele-Shaw
0.01
0.1
1
10
Separation (cm)

Figure 4

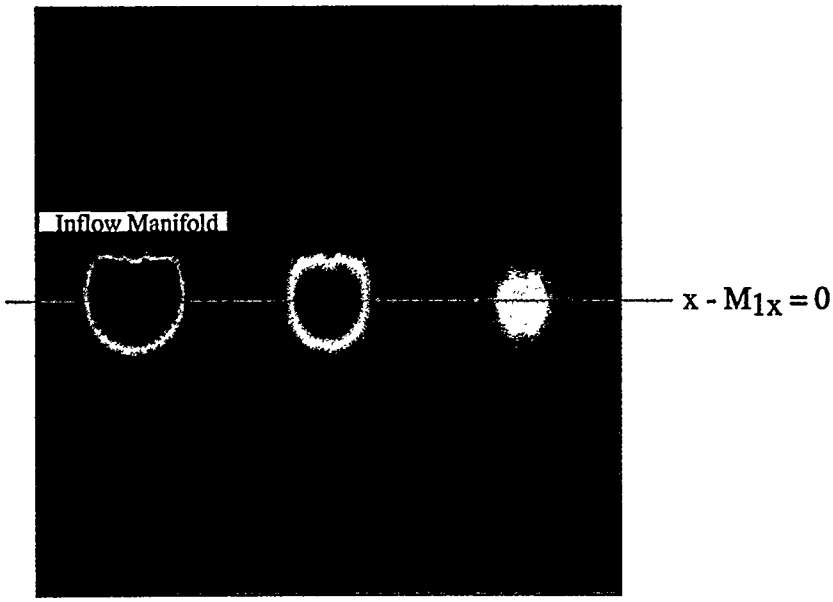

Figure 5a

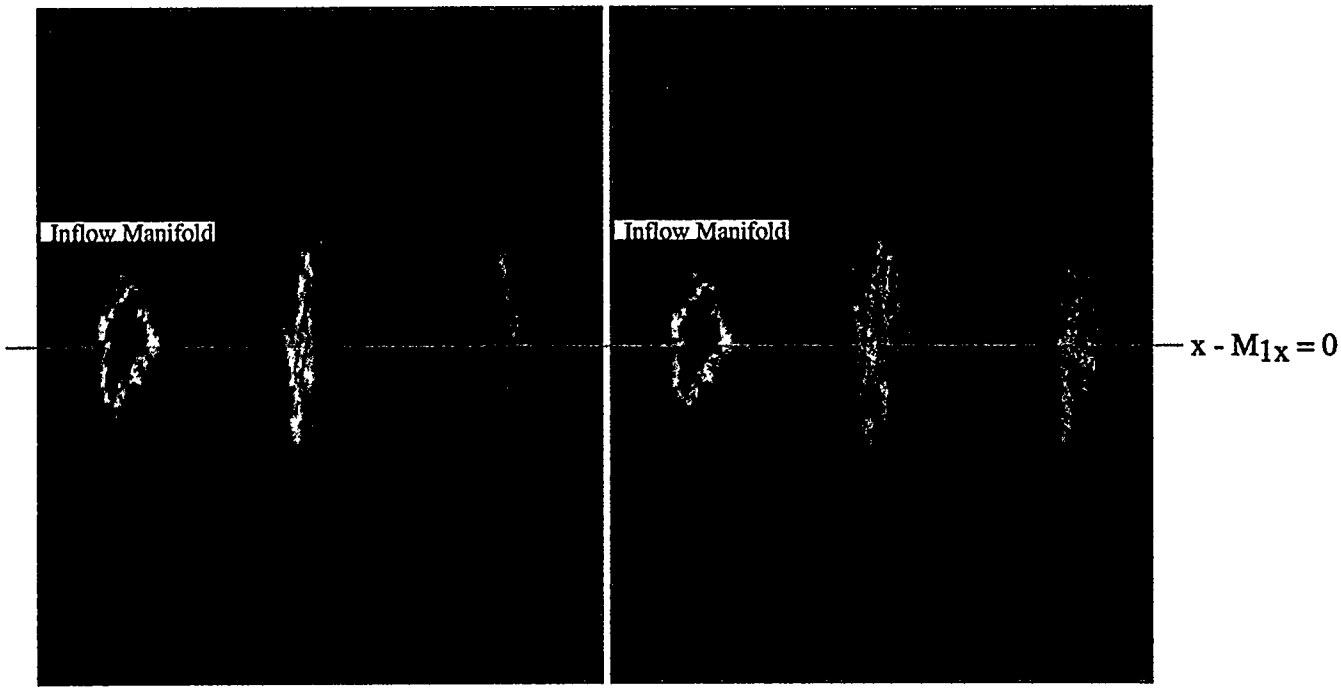

Figure 5b

Figure 5c

C = 0 g/l

C > 0.12 g/l

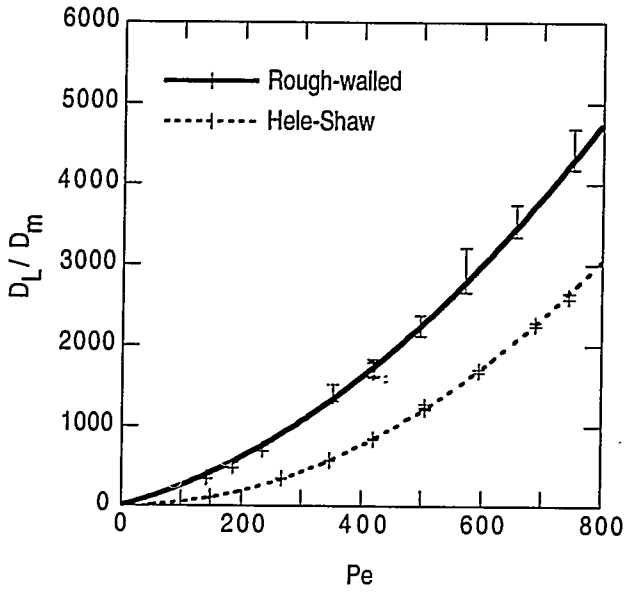
6000
5000
4000
3000
2000
1000
0
D_L / D_m
Rough-walled
Hele-Shaw
0
200
400
600
800
Pe

Figure 6

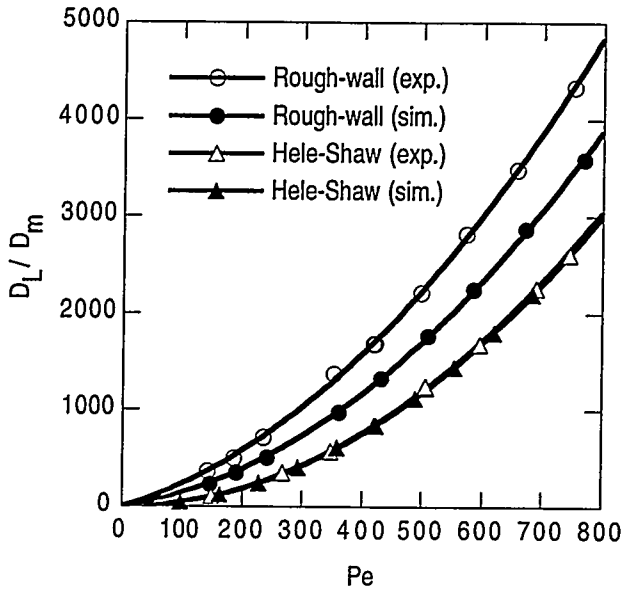
5000
4000
3000
2000
1000
0
D_L / D_m
Rough-wall (exp.)
Rough-wall (sim.)
Hele-Shaw (exp.)
Hele-Shaw (sim.)
0 100 200 300 400 500 600 700 800
Pe

Figure 7

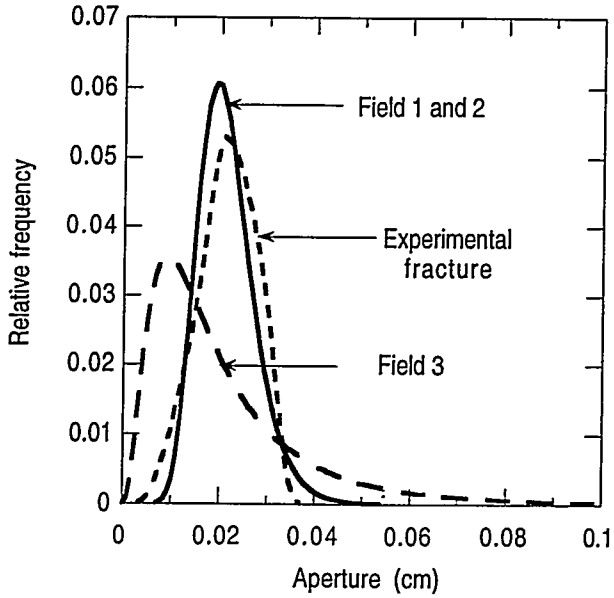
0.07
0.06
0.05
0.04
0.03
0.02
0.01
0
Relative frequency
Field 1 and 2
Experimental fracture
Field 3
0
0.02
0.04
0.06
0.08
0.1
Aperture (cm)

Figure 8

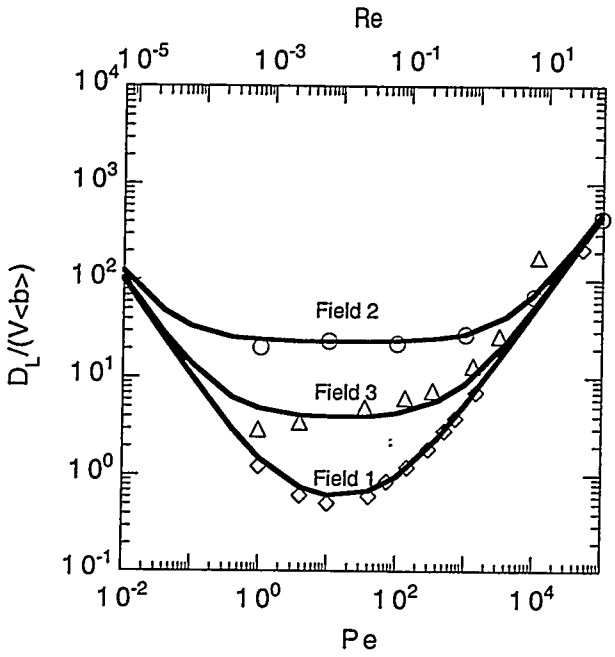
Re
10-5
10-3
10-1
101
104
103
102
101
100
10-1
DL/(V<b>)
Field 2
Field 3
Field 1
10-2
100
102
104
Pe

Figure 9

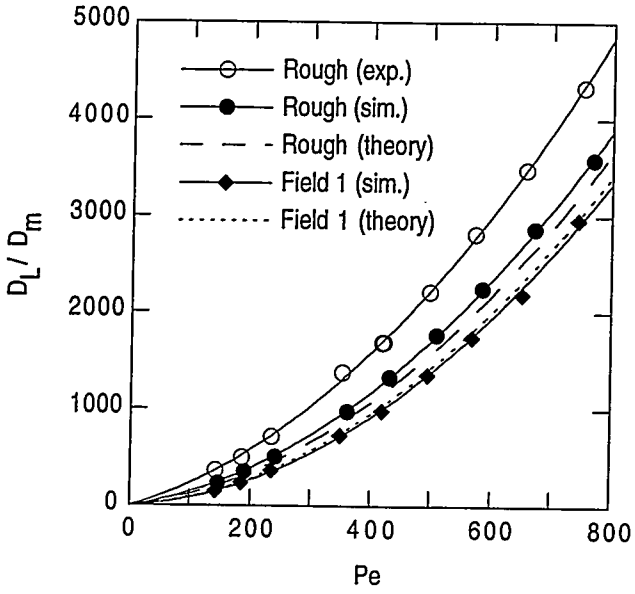
5000
4000
3000
2000
1000
0
0
200
400
600
800
Pe
D_L / D_m
Rough (exp.)
Rough (sim.)
Rough (theory)
Field 1 (sim.)
Field 1 (theory)

Figure 10